Quantum Many-Body Scars beyond the PXP Model in Rydberg Simulators

Aron Kerschbaumer,[1] Marko Ljubotina,[1,2,3] Maksym Serbyn,[1] and Jean-Yves Desaules[1,*]
[1]Institute of Science and Technology Austria (ISTA), Am Campus 1, 3400 Klosterneuburg, Austria
[2]Physics Department, Technical University of Munich, TUM School of Natural Sciences, Lichtenbergstraße 4, Garching 85748, Germany
[3]Munich Center for Quantum Science and Technology (MCQST), Schellingstraße 4, München 80799, Germany

(Received 7 November 2024; accepted 7 March 2025; published 22 April 2025)

Persistent revivals recently observed in Rydberg atom simulators have challenged our understanding of thermalization and attracted much interest to the concept of quantum many-body scars (QMBSs). QMBSs are non-thermal highly excited eigenstates that coexist with typical eigenstates in the spectrum of many-body Hamiltonians, and have since been reported in multiple theoretical models, including the so-called PXP model, approximately realized by Rydberg simulators. At the same time, questions of how common QMBSs are and in what models they are physically realized remain open. In this Letter, we demonstrate that QMBSs exist in a broader family of models that includes and generalizes PXP to longer-range constraints and states with different periodicity. We show that in each model, *multiple* QMBS families can be found. Each of them relies on a different approximate $\mathfrak{su}(2)$ algebra, leading to oscillatory dynamics in all cases. However, in contrast to the PXP model, their observation requires launching dynamics from weakly entangled initial states rather than from a product state. QMBSs reported here may be experimentally probed using Rydberg atom simulator in the regime of longer-range Rydberg blockades.

DOI: 10.1103/PhysRevLett.134.160401

Introduction—Many-body quantum systems generically exhibit fast thermalization, where the system quickly loses memory of initial observables and equilibrates to the state determined only by conserved quantities such as energy. Such behavior can be understood [1] by assuming that eigenstates obey the eigenstate thermalization hypothesis (ETH) [2,3]. The ETH conjectures that the eigenstates themselves behave like thermal states and naturally explains thermalization observed in unitary dynamics. In the examples where interacting quantum systems do not reach a simple thermal state, such as in so-called integrable [4] and many-body localized models [5,6], one typically observes that ETH is also violated by all eigenstates of the system. The strong breakdown of ETH is attributed to the emergence of an extensive number of conserved quantities that constrain the dynamics and impact properties of eigenstates.

More recently, the phenomenon of quantum many-body scars (QMBSs) [7–9] demonstrated a weak breakdown of ETH. QMBSs are defined as eigenstates of interacting quantum systems that violate ETH, while coexisting with other ETH-complying eigenstates at finite energy density. Although such isolated nonthermal eigenstates were previously found in several models [10–12], the experimental observation of persistent revivals in a Rydberg atom quantum simulator [13] and its theoretical understanding through scars [14,15] attracted significant attention.

One of the most emblematic models featuring QMBSs is the so-called PXP model [16,17], that approximately describes the Rydberg atom experiment [13] in the nearest-neighbor blockade regime where scarring occurs. In this limit, each Rydberg atom—viewed as a two-level system—performs Rabi oscillations under a driving field, subject to a blockade condition that prevents adjacent atoms from simultaneously being in the excited state. Theoretically, QMBSs oscillations in the PXP model were linked to an approximate hidden $\mathfrak{su}(2)$ algebra [15,18] or, alternatively, to periodic trajectories in a variational description [19–21]. However, despite a vast amount of research on the PXP model [22–27], its properties are still not fully understood.

In particular, recent works hint at the existence of numerous other approximate QMBSs eigenstates [28,29] in the PXP model. Nevertheless, a simple criterion to determine which states in the PXP model evade thermalization remains missing. Another mystery is the relation between scarring and the nearest-neighbor blockade condition: while generalizations of the PXP model with higher spins [19,30,31] have been numerically shown to host the same type of QMBSs, this was not reported in generalizations of PXP that describe Rydberg arrays in regimes beyond nearest-neighbor blockade [32].

*Contact author: jean-yves.desaules@ist.ac.at

In this Letter, we demonstrate the existence of QMBSs in generalizations of the PXP model to *arbitrary* blockade range. Constructing QMBSs in such generalized models and probing them experimentally relies on initial *short-range entangled* states playing the role of the Néel product state used in the PXP model [13–15]. For the PXP model and its generalizations, we construct three short-range parent states with different periodicity that can be experimentally prepared, and lead to periodic revivals. Thus we broaden the class of physically realizable models, with each of them hosting at least three different families of QMBSs. As an implication of our results, we show that QMBSs-related dynamics can be used to efficiently prepare entangled W states with a size of the order of the blockade range, and conjecture the existence of QMBS in the continuum limit.

Models and properties—The PXP model [16,17], $H_{\mathrm{PXP}} = \sum_{j=1}^{N} P_{j-1}\sigma_j^x P_{j+1}$, is an approximate description of a N-atom Rydberg chain performing Rabi oscillations in the regime of nearest-neighbor blockade. Each Rydberg atom is viewed as an effective spin-1/2 either in the ground ($|\downarrow\rangle$) or excited Rydberg ($|\uparrow\rangle$) state, and the Pauli matrix σ_i^x generates Rabi oscillations. Since atoms interact only in their Rydberg ($|\uparrow\rangle$) states, tuning the interatom distance can prevent nearest-neighbor excitations via the Rydberg blockade. In the PXP Hamiltonian, this condition is implemented using the projector $P = |\downarrow\rangle\langle\downarrow|$.

While the PXP Hamiltonian is nonintegrable [14,34–36], it features a family of QMBSs related to the Néel state $|\mathbf{Z}_2\rangle = |\downarrow\uparrow\downarrow\uparrow\ldots\downarrow\uparrow\rangle$ [37]. QMBSs are approximately contained in the subspace that can be generated by the action of a simple raising operator onto the Néel state—a manifestation of an approximate $\mathfrak{su}(2)$ algebra [18,38]. Consequently, unitary dynamics launched from the Néel state leads to coherent oscillations between $|\mathbf{Z}_2\rangle$ and $|\mathbf{Z}_2'\rangle = |\uparrow\downarrow\uparrow\downarrow\ldots\uparrow\downarrow\rangle$. Revivals can also be seen from the period-3 state $|\mathbf{Z}_3\rangle = |\downarrow\downarrow\uparrow\downarrow\downarrow\uparrow\ldots\downarrow\downarrow\uparrow\rangle$. However, $|\mathbf{Z}_n\rangle$ states with $n > 3$ equilibrate quickly despite their similar structure.

We generalize the PXP model to blockade radius α as follows:

$$H_\alpha = \sum_{j=1}^{N} P_{j-\alpha}\ldots P_{j-1}\sigma_j^x P_{j+1}\ldots P_{j+\alpha} = \sum_{j=1}^{N} \tilde{\sigma}_j^x, \quad (1)$$

which can be approximately realized experimentally; see End Matter. This model is the focus of this work and reduces to H_{PXP} when $\alpha = 1$. Here and in the rest of this Letter, we use $\tilde{\sigma}_j^x$ as a shorthand notation for σ_j^x dressed with α projectors on each side. We also assume periodic boundary conditions (PBC) unless stated otherwise. For brevity, we generally suppress α except in H_α.

The Hamiltonian (1) is chaotic for generic α and a few isolated exact scars are known [36,39]. However, these scarred eigenstates do not admit an algebraic description and no simple reviving state was reported for $\alpha > 1$. Even $|\mathbf{Z}_{\alpha+1}\rangle$, the natural generalization of $|\mathbf{Z}_2\rangle$ to $\alpha > 1$, displays fast thermalization under dynamics generated by H_α. Intuitively, this absence of revivals can be attributed to *frustration*. For $\alpha = 1$ the Néel state $|\mathbf{Z}_2\rangle$ has a unique partner $|\mathbf{Z}_2'\rangle$ under translation, leading to oscillations between these two states. However, for $\alpha \geq 2$, $|\mathbf{Z}_{\alpha+1}\rangle$ has α translated partners. A superposition of these states cannot serve as the unique partner state for $|\mathbf{Z}_{\alpha+1}\rangle$ since finite-time dynamics is incapable of transforming a given product state into a catlike superposition of macroscopically different states, resulting in frustration. Below, we argue that introducing short-range entanglement in the initial state lifts this frustration [40–42] as it allows to create new pairs of states between which scarred dynamics is possible.

Lifting frustration by entanglement—We propose a different way of generalizing the Néel state for an even unit-cell size K (we discuss the odd case below). We define the state $|K\rangle$ with M repeating unit cells of size K as

$$|K\rangle = \bigotimes_{j=1}^{M} [|0\rangle_{K/2} \otimes |W\rangle_{K/2}], \quad (2)$$

which is built from the product state $|0\rangle_{K/2} = |\downarrow\ldots\downarrow\rangle$, in the first half of the unit cell, and the entangled W state, $|W\rangle_{K/2} = \sqrt{2/K}(|\uparrow\downarrow\cdots\downarrow\rangle + |\downarrow\uparrow\downarrow\cdots\downarrow\rangle + \cdots + |\downarrow\cdots\downarrow\uparrow\rangle)$, where one $\uparrow$-spin is uniformly distributed in the second half of the unit cell. This short-range entangled state can be written as a matrix product state (MPS) with bond dimension $\chi = 2$ for $K > 2$ and reduces to the Néel state for $K = 2$. Below we demonstrate that this state lifts frustration, such that it is approximately transformed into its reflected version $|K'\rangle = I|K\rangle$ (with I the spatial reflection operator) with unit cell $|W\rangle_{K/2} \otimes |0\rangle_{K/2}$ under the unitary dynamics generated by H_α.

Figure 1(a) shows that for a period $K = 6$ unit cell, the $|K\rangle$ state has strong revivals in models with $\alpha = 2$ and $\alpha = 3$. These revivals are indicative of the presence of QMBSs [43]. QMBSs become apparent in Figs. 1(b)–1(e), which show the overlap of eigenstates of $H_{\alpha=2,3}$ with the $|K\rangle$ state as well as their entanglement entropy. A set of approximately equally spaced eigenstates is clearly visible with enhanced overlap and low entanglement.

For a chain of length N, QMBSs appear at $2N/K + 1$ special energies, i.e., twice the number of unit cells plus one. However, there are more scarred eigenstates as some of them are degenerate, see SM [44]. This number of scarred energies can be understood by considering every cell as an effective two-level system oscillating between $|0\rangle_{K/2} \otimes |W\rangle_{K/2} \equiv |\Downarrow\Uparrow\rangle$ and $|W\rangle_{K/2} \otimes |0\rangle_{K/2} \equiv |\Uparrow\Downarrow\rangle$, providing an approximate mapping to the PXP $|\mathbf{Z}_2\rangle$ case with $|0\rangle \rightleftharpoons |\Downarrow\rangle$ and $|W\rangle \rightleftharpoons |\Uparrow\rangle$. For such a mapping to work, the Rydberg blockade must be effective within the range of

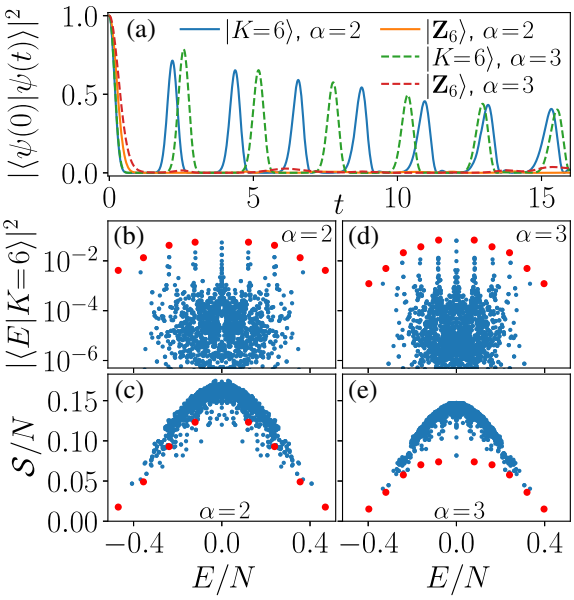

FIG. 1. QMBSs with longer-range blockade $\alpha = 2$ and 3 obtained from the $|K = 6\rangle$ state. (a) Time evolution after a quench shows good revivals for the $|K = 6\rangle$ state and no revivals for the product state $|\mathbf{Z}_6\rangle$. Overlap of eigenstates with $|K = 6\rangle$ in (b) and (d) as well as half-chain von Neumann entanglement entropy S of the eigenstates in (c) and (e) show QMBSs as outliers, that are highlighted in red and coincide in plots (b),(c) and (d),(e). Data shown is for system sizes $N = 24, 30$ (for $\alpha = 2$, 3 respectively) and all relevant momentum sectors.

$K/2$: the application of H_α to the state $|W\rangle_{K/2}$ should yield the $|0\rangle_{K/2}$ state and not be able to create additional $|\uparrow\rangle$-excitations. This leads to an upper bound on the unit cell size, $K/2 \leq \alpha + 1$. In addition, we obtain the lower bound $K \geq 2\alpha$, since values of K below 2α cause excitations in adjacent $|W\rangle_{K/2}$ states to violate the blockade condition. This leaves only *three* possible values of the unit cell size K for a given α, $K = 2\alpha$, $K = 2\alpha + 1$, and $K = 2\alpha + 2$. We first consider even K and later generalize to $K = 2\alpha + 1$.

Algebraic description—To devise the $\mathfrak{su}(2)$ algebra, we generalize the forward scattering approximation (FSA) introduced for the PXP model [14]. We set the global raising operator J^+ such that $J^+ + J^- = H_\alpha$ and $J^-|K\rangle = 0$, where $J^- := (J^+)^\dagger$. This implies that J^+ acts with $\tilde{\sigma}^+$ on sites within $|0\rangle_{K/2}$ in Eq. (2) and as $\tilde{\sigma}^-$ on sites within $|W\rangle_{K/2}$. These operators are related by inversion, $J^- = IJ^+I$. They allow us to define the rest of the algebra, with $J^x = (J^+ + J^-)/2 = H_\alpha/2$ and

$$J^y = \frac{1}{2i}(J^+ - J^-) = \frac{1}{2}\sum_{j=1}^{N} f(j)\tilde{\sigma}_j^y \tag{3}$$

being the sum of $\tilde{\sigma}^y$ operators with positive (negative) $f(j) = \pm 1$ signs on the first (last) $K/2$ sites of each unit cell.

We obtain the z component of the collective spin as $J^z = [J^x, J^y]/i$. It has $\tilde{\sigma}^z$ terms with the same $f(j)$ sign structure as in J^y. This favors $|\downarrow\rangle$ in the first half of each cell and $|\uparrow\rangle$ in the second half. Unlike in the PXP $\mathbf{Z}_2$ case, J^z also has XY-type terms $f(j)(\tilde{\sigma}_j^+\tilde{\sigma}_k^- + \tilde{\sigma}_k^+\tilde{\sigma}_j^-)$. Crucially, for $K = 2\alpha$ or $2\alpha + 2$ these terms act between *all* sites in the second half of the cell, favoring $|W\rangle$ over any other combination of states with a single $|\uparrow\rangle$. As a consequence, the ground state $|\mathrm{GS}_z\rangle$ of J^z is approximately equal to $|K\rangle$ ($\approx$0.98 overlap for the cases of α and N shown in Fig. 1), thus providing a self-consistent check of this algebra. Meanwhile, for other (even) values of K, the XY terms have a different structure and the overlap between $|\mathrm{GS}_z\rangle$ and $|K\rangle$ drops quickly.

From the algebraic picture, we can understand the revivals as the precession of a collective spin of size N/K. Starting from $|K\rangle \approx |\mathrm{GS}_z\rangle$, the Hamiltonian—which is proportional to J^x—will lead to a rotation in the yz plane along the Bloch sphere. We then expect the wave function to pass close to the ceiling state $|\mathrm{CS}_y\rangle$ of J^y, the ceiling state $|\mathrm{CS}_z\rangle = I|\mathrm{GS}_z\rangle \approx |K'\rangle$ of J^z, the ground state $|\mathrm{GS}_y\rangle = I|\mathrm{CS}_y\rangle$ of J^y, before coming back to $|\mathrm{GS}_z\rangle$, as indicated in Fig. 2(a).

Our ansatz for the algebra can be extended to odd values of K by acting with $\tilde{\sigma}^x/2$ (instead of $\tilde{\sigma}^\pm$) on the middle site of each unit cell in J^+. This preserves the property $IJ^+I = J^- := (J^+)^\dagger$. The remaining operators of the approximate $\mathfrak{su}(2)$ algebra are constructed as for even K above. We leave the details to End Matter and focus on the ground state of J^z, which is approximately

$$|K\rangle = \bigotimes_{j=1}^{M}[|0\rangle_\alpha \otimes |\tilde{W}_\beta\rangle_{\alpha+1}], \tag{4}$$

for $K = 2\alpha + 1$. The deformed W-state $|\tilde{W}_\beta\rangle_{\alpha+1} = [\beta|\uparrow\rangle|0\rangle_\alpha + \sqrt{\alpha}|\downarrow\rangle|W\rangle_\alpha]/\sqrt{|\beta|^2 + \alpha}$ (with a numerically determined optimal value of $\beta \approx 0.65$), also contains superpositions of all possible one-spin excitations within the block of $\alpha + 1$ sites, but the weight of excitation on the first

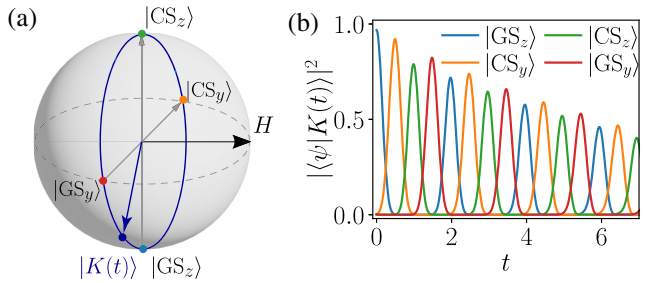

FIG. 2. (a) Collective-spin picture of the dynamics. Starting from $|K\rangle \approx |\mathrm{GS}_z\rangle$, we expect the Hamiltonian (proportional to J^x) to generate precession in the yz plane, passing through the ground and ceiling states of J^y and J^z. This dynamics is illustrated by plotting fidelities for $\alpha = 4$, $K = 9$, and $N = 36$ in panel (b).

spin is now suppressed. Figure 2(b) shows that a quench from state (4) leads to strong oscillatory dynamics, as was the case for $K = 2\alpha$ and $K = 2\alpha + 2$. Furthermore, the overlap with the ground and ceiling states of J^y and J^z demonstrates that the picture of precession of a large spin offered by the approximate $\mathfrak{su}(2)$ algebra holds well.

Inspired by this description, we develop an MPS variational manifold akin to spin coherent states projected in the constrained Hilbert space [19,20]. In End Matter, we present evidence of the existence of periodic trajectories in this semiclassical limit for $\alpha = 1$ and $\alpha = 2$, with a period $K = 4$ unit cell using MPS with bond dimension $\chi = 2$ and $\chi = 3$ respectively. We conjecture that such trajectories exist for any blockade range.

Implications for scars in PXP—The $|K\rangle$ states constructed in Eqs. (2) and (4) also have nontrivial implications for QMBSs in the PXP model, $\alpha = 1$. In that model, a weakly entangled period-3 initial state was known to have revivals better than $|\mathbf{Z}_3\rangle$ [20]. Our approach elucidates its origin, as we find that it corresponds to the ground state of J^y. In contrast, revivals from period-4 states in the PXP model were not reported previously. This is explained by the small overlap of $|\mathbf{Z}_4\rangle$ on the proper reviving state built from the size-4 unit cell $|\downarrow\downarrow\rangle[|\uparrow\downarrow\rangle + |\uparrow\downarrow\rangle]/\sqrt{2}$ [cf. with Eq. (2) for $\alpha = 1$ and $K = 4$]. For instance, for $N = 24$ the overlap of $|\mathbf{Z}_4\rangle$ with the period-4 state Eq. (2) is very small $0.841^N \approx 0.0156$, whereas $|\mathbf{Z}_3\rangle$ has considerable overlap with the best reviving period-3 state at $0.956^N \approx 0.336$ [44].

Revivals across different blockade ranges—We compare dynamics for the reviving states found above across different α. Figure 3 shows clear fidelity revivals after quenches from the $|K\rangle$ state for $\alpha = 1, \ldots, 6$ and the three special unit cell sizes discussed above. Importantly, the revival period scales approximately as $1/\sqrt{K/2 + C}$. This can be understood from the approximate mapping to the PXP $|\mathbf{Z}_2\rangle$ case using an effective two-level system. Mapping $|W\rangle_{K/2}$ to $|\Uparrow\rangle$ and $|0\rangle_{K/2}$ to $|\Downarrow\rangle$ gives the $|\mathbf{Z}_2\rangle$ state of effective spins, but the matrix element of the Hamiltonian is now $\langle\Uparrow|H_\alpha|\Downarrow\rangle = \sqrt{K/2}$. This implies a scaling of the revival period as $\sqrt{2/K}$ without any corrections. However, this mapping is only approximate, and numerically we find that $C \approx -0.15$ for $K = 2\alpha$ and $2\alpha + 1$, and $C \approx 0.75$ for $K = 2\alpha + 2$.

Next, we compare revivals across a much broader range of unit cell sizes, $\alpha + 1 \leq K \leq 2\alpha + 4$ for different α. Note that the initial state $|K\rangle$ violates the blockade condition for $K < 2\alpha$, hence we project it back onto the constrained subspace. Revivals can be quantified in a system-size independent way using the fidelity density f_1 as this quantity quickly converges with N [44]. Fidelity density is defined as $f_1 = -\ln(\mathcal{F}_1)/N$, where $\mathcal{F}_1 = |\langle K|e^{-iTH_\alpha}|K\rangle|^2$ is the fidelity at the time of the first revival. However, we also have to account for the varying constraint as α is changed, which is achieved by using a

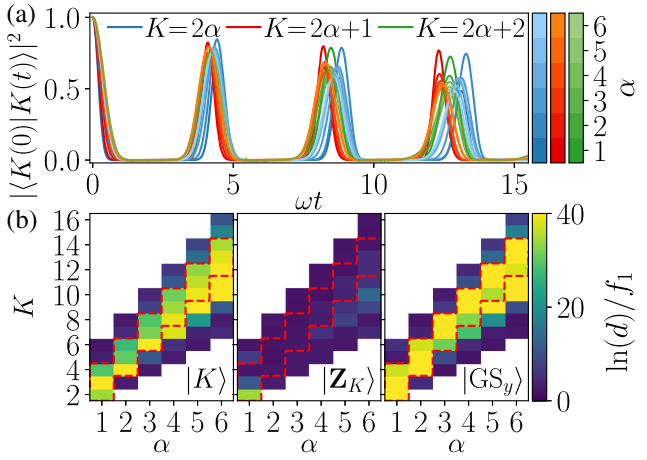

FIG. 3. (a) Fidelity after quenches from the $|K\rangle$ state for $2\alpha \leq K \leq 2\alpha + 2$. Time is rescaled by $\omega = \sqrt{K/2 + C}$, with $C = -0.15$ for $K \leq 2\alpha + 1$ and $C = 0.75$ for $K = 2\alpha + 2$. (b) Inverse fidelity density f_1 times the logarithm of the quantum dimension d for three different initial states. A large value indicates clear revivals. The red dashed lines denote the range between $K = 2\alpha$ and $K = 2\alpha + 2$. In the domain they delimit, good revivals can be seen for all α for $|K\rangle$ and $|\mathrm{GS}_y\rangle$, but not for $|\mathbf{Z}_K\rangle$. The system sizes used and the data for fidelity can be found in SM [44].

normalized inverse fidelity density, $\ln(d)/f_1$, with d the effective local Hilbert space dimension (such that the Hilbert size is $\sim d^N$ [44]). The quantity $\ln(d)/f_1$ is expected to be of order one for a thermalizing state, and much larger than one in the case of strong revivals, indicating ergodicity breaking. For large α, Fig. 3(b) shows revivals not only for the three special values of K, but also for $K < 2\alpha$. In contrast, for $K > 2\alpha + 2$ the revivals disappear rapidly. We conjecture that the revivals for $K < 2\alpha$ can be understood in a similar fashion, but with initial states presenting longer-range correlations.

Figure 3(b) also shows that initial product states do not have clear revivals except for $|\mathbf{Z}_2\rangle$ in the PXP model, whereas the initial $|\mathrm{GS}_y\rangle$ state obtained from $\mathfrak{su}(2)$ algebra has revivals that are stronger compared to the $|K\rangle$ initial state (in particular for $K = 2\alpha + 1$, see SM [44]). Below we use the good revivals of $|\mathrm{GS}_y\rangle$ to devise an experimental protocol for probing QMBSs.

Experimental implementation—We focus on the Hamiltonian H_2 from Eq. (1) that can be approximately implemented using a triangular ladder of Rydberg atoms, see inset in Fig. 4(a). Next, we propose to prepare the ground state of the J^y operator in Eq. (3), $|\mathrm{GS}_y\rangle$, instead of $|K\rangle$ from Eq. (2). This state is also a point on the trajectory of the dynamics launched from the $|K\rangle$ state, see Fig. 2(b), and it can be naturally prepared from the ground state of H_2 (obtainable via annealing [13,45]) by single-site unitary rotations ($\pm\pi/2$ pulses in the z direction).

The time evolution with H_2 from the $|\mathrm{GS}_y\rangle$ state is expected to give long-time coherent oscillations,

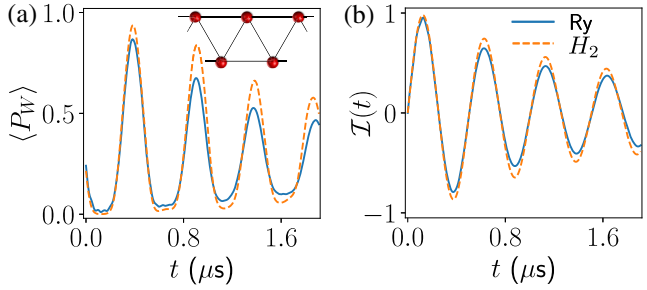

FIG. 4. (a) Expectation value of the projector onto a local W-state and imbalance (b) show long time coherent dynamics, with only a small difference between the approximate H_2 Hamiltonian with (dashed lines) and the realistic Ising-type Hamiltonian of Rydberg atoms arranged into a triangular ladder (see inset and End Matter) with $N = 20$ sites and OBC.

approximately passing different points on the collective spin orbit in Fig. 2(b). After a quarter period, the unitary dynamics will approximately lead to the $|K\rangle$ state, which in this case consists of W states of range two interlaced by product states. Figure 4(a) confirms these expectations by showing the expectation value of the projector onto a two-site W-state, $P_W = (|\uparrow\downarrow\rangle + |\downarrow\uparrow\rangle)(\langle\uparrow\downarrow| + \langle\downarrow\uparrow|)/2$ that reaches a value close to one after a quarter period. The dynamics of the average local imbalance $\mathcal{I} = (4/N)\sum_{j=0}^{N/4-1}[\langle n_{4j+3}\rangle + \langle n_{4j+4}\rangle - \langle n_{4j+1}\rangle - \langle n_{4j+2}\rangle]$ shown in Fig. 4(b) also features coherent oscillations. Notably, the dynamics generated by the approximate H_2 Hamiltonian and by the Ising Hamiltonian for Rydberg atoms arranged into a triangular ladder, where the range-two Rydberg blockade effectively emerges, are similar.

Conclusion and outlook—We demonstrated the existence of new families of QMBSs in longer-range generalizations of the PXP model up to a blockade radius of six. This leads to a natural conjecture that this phenomenon persists for an arbitrary blockade radius. We constructed an effective description of the dynamics in terms of a collective $\mathfrak{su}(2)$ spin, and argued that in order to lift frustration, the QMBSs and nonergodic dynamics must originate from weakly entangled initial states. We also confirmed the existence of "semiclassical" periodic trajectories in variational dynamics over MPS [19,20], thus contributing to the ongoing discussion on the similarities between QMBSs in PXP-type models and scars in models with a more physical classical limit, both in single-[46] and many-body [47–51] quantum systems.

Our work opens the door to the study of QMBSs and weak ergodicity breaking in Rydberg models with longer-range blockades, and of potential stabilization via deformations [18,34,38,52] or driving [53,54]. Although ground state properties were studied for these models [45,55–58], excited state dynamics received little attention. More importantly, our results suggest that QMBSs may be more commonly related to initial weakly entangled states, in agreement with the understanding of QMBSs as originating from periodic trajectories that generally do not pass through product states [19,20]. Moreover, our generalization of QMBSs to a family of models with an arbitrary blockade range suggests a possible extension to continuous (nonlattice) model with QMBSs.

Acknowledgments—The authors are grateful to Zlatko Papić, Dolev Bluvstein, Nishad Maskara, Marcello Dalmonte, Thomas Iadecola, and Johannes Feldmeier for insightful discussions. A. K., M. L., and M. S. acknowledge support by the European Research Council under the European Union's Horizon 2020 research and innovation program (Grant Agreement No. 850899). J.-Y. D. acknowledges funding from the European Union's Horizon 2020 research and innovation program under the Marie Skłodowska-Curie Grant Agreement No. 101034413.

[1] A. P. Luca D'Alessio, Yariv Kafri, and M. Rigol, From quantum chaos and eigenstate thermalization to statistical mechanics and thermodynamics, Adv. Phys. **65**, 239 (2016).
[2] M. Srednicki, Chaos and quantum thermalization, Phys. Rev. E **50**, 888 (1994).
[3] J. M. Deutsch, Eigenstate thermalization hypothesis, Rep. Prog. Phys. **81**, 082001 (2018).
[4] B. Sutherland, *Beautiful Models: 70 Years of Exactly Solved Quantum Many-Body Problems* (World Scientific Publishing Company, Singapore, 2004).
[5] D. A. Abanin, E. Altman, I. Bloch, and M. Serbyn, Colloquium: Many-body localization, thermalization, and entanglement, Rev. Mod. Phys. **91**, 021001 (2019).
[6] R. Nandkishore and D. A. Huse, Many-body localization and thermalization in quantum statistical mechanics, Annu. Rev. Condens. Matter Phys. **6**, 15 (2015).
[7] M. Serbyn, D. A. Abanin, and Z. Papić, Quantum many-body scars and weak breaking of ergodicity, Nat. Phys. **17**, 675 (2021).
[8] A. Chandran, T. Iadecola, V. Khemani, and R. Moessner, Quantum many-body scars: A quasiparticle perspective, Annu. Rev. Condens. Matter Phys. **14**, 443 (2023).
[9] S. Moudgalya, B. A. Bernevig, and N. Regnault, Quantum many-body scars and Hilbert space fragmentation: A review of exact results, Rep. Prog. Phys. **85**, 086501 (2022).
[10] D. P. Arovas, Two exact excited states for the $S = 1$ AKLT chain, Phys. Lett. A **137**, 431 (1989).
[11] N. Shiraishi and T. Mori, Systematic construction of counterexamples to the eigenstate thermalization hypothesis, Phys. Rev. Lett. **119**, 030601 (2017).
[12] S. Moudgalya, N. Regnault, and B. A. Bernevig, Entanglement of exact excited states of Affleck-Kennedy-Lieb-Tasaki models: Exact results, many-body scars, and violation of the strong eigenstate thermalization hypothesis, Phys. Rev. B **98**, 235156 (2018).
[13] H. Bernien, S. Schwartz, A. Keesling, H. Levine, A. Omran, H. Pichler, S. Choi, A. S. Zibrov, M. Endres, M. Greiner *et al.*, Probing many-body dynamics on a 51-atom quantum simulator, Nature (London) **551**, 579 (2017).

[14] C. J. Turner, A. A. Michailidis, D. A. Abanin, M. Serbyn, and Z. Papić, Weak ergodicity breaking from quantum many-body scars, Nat. Phys. **14**, 745 (2018).
[15] C. J. Turner, A. A. Michailidis, D. A. Abanin, M. Serbyn, and Z. Papić, Quantum scarred eigenstates in a Rydberg atom chain: Entanglement, breakdown of thermalization, and stability to perturbations, Phys. Rev. B **98**, 155134 (2018).
[16] I. Lesanovsky and H. Katsura, Interacting Fibonacci anyons in a Rydberg gas, Phys. Rev. A **86**, 041601(R) (2012).
[17] P. Fendley, K. Sengupta, and S. Sachdev, Competing density-wave orders in a one-dimensional hard-boson model, Phys. Rev. B **69**, 075106 (2004).
[18] S. Choi, C. J. Turner, H. Pichler, W. W. Ho, A. A. Michailidis, Z. Papić, M. Serbyn, M. D. Lukin, and D. A. Abanin, Emergent SU(2) dynamics and perfect quantum many-body scars, Phys. Rev. Lett. **122**, 220603 (2019).
[19] W. W. Ho, S. Choi, H. Pichler, and M. D. Lukin, Periodic orbits, entanglement, and quantum many-body scars in constrained models: Matrix product state approach, Phys. Rev. Lett. **122**, 040603 (2019).
[20] A. A. Michailidis, C. J. Turner, Z. Papić, D. A. Abanin, and M. Serbyn, Slow quantum thermalization and many-body revivals from mixed phase space, Phys. Rev. X **10**, 011055 (2020).
[21] C. J. Turner, J.-Y. Desaules, K. Bull, and Z. Papić, Correspondence principle for many-body scars in ultracold Rydberg atoms, Phys. Rev. X **11**, 021021 (2021).
[22] F. M. Surace, P. P. Mazza, G. Giudici, A. Lerose, A. Gambassi, and M. Dalmonte, Lattice gauge theories and string dynamics in Rydberg atom quantum simulators, Phys. Rev. X **10**, 021041 (2020).
[23] T. Iadecola, M. Schecter, and S. Xu, Quantum many-body scars from magnon condensation, Phys. Rev. B **100**, 184312 (2019).
[24] C.-J. Lin and O. I. Motrunich, Exact quantum many-body scar states in the Rydberg-blockaded atom chain, Phys. Rev. Lett. **122**, 173401 (2019).
[25] P.-G. Rozon, M. J. Gullans, and K. Agarwal, Constructing quantum many-body scar Hamiltonians from Floquet automata, Phys. Rev. B **106**, 184304 (2022).
[26] G. Giudici, F. M. Surace, and H. Pichler, Unraveling PXP many-body scars through Floquet dynamics, Phys. Rev. Lett. **133**, 190404 (2024).
[27] B. Windt and H. Pichler, Squeezing quantum many-body scars, Phys. Rev. Lett. **128**, 090606 (2022).
[28] T. Szołdra, P. Sierant, M. Lewenstein, and J. Zakrzewski, Unsupervised detection of decoupled subspaces: Many-body scars and beyond, Phys. Rev. B **105**, 224205 (2022).
[29] M. Ljubotina, J.-Y. Desaules, M. Serbyn, and Z. Papić, Superdiffusive energy transport in kinetically constrained models, Phys. Rev. X **13**, 011033 (2023).
[30] J.-Y. Desaules, A. Hudomal, D. Banerjee, A. Sen, Z. Papić, and J. C. Halimeh, Prominent quantum many-body scars in a truncated Schwinger model, Phys. Rev. B **107**, 205112 (2023).
[31] J.-Y. Desaules, D. Banerjee, A. Hudomal, Z. Papić, A. Sen, and J. C. Halimeh, Weak ergodicity breaking in the Schwinger model, Phys. Rev. B **107**, L201105 (2023).
[32] In contrast, scarring due to Hilbert-space fragmentation was observed in Rydberg atoms in the regime of anti-blockade [33].
[33] L. Zhao, P. R. Datla, W. Tian, M. M. Aliyu, and H. Loh, Observation of quantum thermalization restricted to Hilbert space fragments, Phys. Rev. X **15**, 011035 (2025).
[34] V. Khemani, C. R. Laumann, and A. Chandran, Signatures of integrability in the dynamics of Rydberg-blockaded chains, Phys. Rev. B **99**, 161101(R) (2019).
[35] H. K. Park and S. Lee, Proof of the nonintegrability of the PXP model and general spin-1/2 systems, arXiv:2403.02335.
[36] L. Corcoran, M. de Leeuw, and B. Pozsgay, Integrable models on Rydberg atom chains, arXiv:2405.15848.
[37] In this work, we will use the convention for all $\mathbf{Z}_d$ type states that the up-spin is located at the rightmost site of the unit-cell.
[38] K. Bull, J.-Y. Desaules, and Z. Papić, Quantum scars as embeddings of weakly broken Lie algebra representations, Phys. Rev. B **101**, 165139 (2020).
[39] F. M. Surace, M. Votto, E. G. Lazo, A. Silva, M. Dalmonte, and G. Giudici, Exact many-body scars and their stability in constrained quantum chains, Phys. Rev. B **103**, 104302 (2021).
[40] J. I. Cirac, D. Pérez-García, N. Schuch, and F. Verstraete, Matrix product states and projected entangled pair states: Concepts, symmetries, theorems, Rev. Mod. Phys. **93**, 045003 (2021).
[41] C. M. Dawson and M. A. Nielsen, Frustration, interaction strength, and ground-state entanglement in complex quantum systems, Phys. Rev. A **69**, 052316 (2004).
[42] J. Preskill, Quantum information and physics: Some future directions, J. Mod. Opt. **47**, 127 (2000).
[43] A. M. Alhambra, A. Anshu, and H. Wilming, Revivals imply quantum many-body scars, Phys. Rev. B **101**, 205107 (2020).
[44] See Supplemental Material at http://link.aps.org/supplemental/10.1103/PhysRevLett.134.160401 for additional results and details, which include Refs. [14,15,18,23,38].
[45] A. Keesling, A. Omran, H. Levine, H. Bernien, H. Pichler, S. Choi, R. Samajdar, S. Schwartz, P. Silvi, S. Sachdev, P. Zoller, M. Endres, M. Greiner, V. Vuletić, and M. D. Lukin, Quantum Kibble–Zurek mechanism and critical dynamics on a programmable Rydberg simulator, Nature (London) **568**, 207 (2019).
[46] E. J. Heller, Bound-state eigenfunctions of classically chaotic Hamiltonian systems: Scars of periodic orbits, Phys. Rev. Lett. **53**, 1515 (1984).
[47] S. Pilatowsky-Cameo, D. Villaseñor, M. A. Bastarrachea-Magnani, S. Lerma-Hernández, L. F. Santos, and J. G. Hirsch, Ubiquitous quantum scarring does not prevent ergodicity, Nat. Commun. **12**, 852 (2021).
[48] B. Evrard, A. Pizzi, S. I. Mistakidis, and C. B. Dag, Quantum scars and regular eigenstates in a chaotic spinor condensate, Phys. Rev. Lett. **132**, 020401 (2024).
[49] Q. Hummel, K. Richter, and P. Schlagheck, Genuine many-body quantum scars along unstable modes in Bose-Hubbard systems, Phys. Rev. Lett. **130**, 250402 (2023).

[50] A. Pizzi, B. Evrard, C. B. Dag, and J. Knolle, Quantum scars in many-body systems, arXiv:2408.10301.
[51] I. Ermakov, O. Lychkovskiy, and B. V. Fine, Periodic classical trajectories and quantum scars in many-spin systems, arXiv:2409.00258.
[52] K. Omiya and M. Müller, Quantum many-body scars in bipartite Rydberg arrays originating from hidden projector embedding, Phys. Rev. A **107**, 023318 (2023).
[53] D. Bluvstein, A. Omran, H. Levine, A. Keesling, G. Semeghini, S. Ebadi, T. T. Wang, A. A. Michailidis, N. Maskara, W. W. Ho *et al.*, Controlling quantum many-body dynamics in driven Rydberg atom arrays, Science **371**, 1355 (2021).
[54] N. Maskara, A. A. Michailidis, W. W. Ho, D. Bluvstein, S. Choi, M. D. Lukin, and M. Serbyn, Discrete time-crystalline order enabled by quantum many-body scars: Entanglement steering via periodic driving, Phys. Rev. Lett. **127**, 090602 (2021).
[55] R. Samajdar, W. W. Ho, H. Pichler, M. D. Lukin, and S. Sachdev, Complex density wave orders and quantum phase transitions in a model of square-lattice Rydberg atom arrays, Phys. Rev. Lett. **124**, 103601 (2020).
[56] N. Chepiga and F. Mila, Kibble-Zurek exponent and chiral transition of the period-4 phase of Rydberg chains, Nat. Commun. **12**, 414 (2021).
[57] N. Chepiga and F. Mila, Lifshitz point at commensurate melting of chains of Rydberg atoms, Phys. Rev. Res. **3**, 023049 (2021).
[58] I. A. Maceira, N. Chepiga, and F. Mila, Conformal and chiral phase transitions in Rydberg chains, Phys. Rev. Res. **4**, 043102 (2022).
[59] G. Vidal, Classical simulation of infinite-size quantum lattice systems in one spatial dimension, Phys. Rev. Lett. **98**, 070201 (2007).
[60] U. Schollwöck, The density-matrix renormalization group in the age of matrix product states, Ann. Phys. (Amsterdam) **326**, 96 (2011).

End Matter

Experimental setup—The experimental Hamiltonian we consider is

$$\frac{1}{\hbar}H_{\mathrm{exp}} = \frac{\Omega}{2}\sum_{j=1}^{N}\sigma_j^x - \Delta\sum_{j=1}^{N}n_j + V_1\sum_{\substack{j,k=1\\ j<k}}^{N}\frac{n_j n_k}{d_{j,k}^6}, \tag{A1}$$

where $d_{j,k} = ||\vec{r}_j - \vec{r}_k||_2/a$ is the distance between atoms j and k in units of the lattice spacing a. The Rydberg blockade prevents excitation within the blockade distance R_b, defined by $\Omega = V_1(a/R_b)^6$ [13]. Choosing the lattice spacing $R_b/(\alpha+1) < a < R_b/\alpha$ then approximates the Hamiltonian in Eq. (1). However, for large α, maintaining a strong blockade while suppressing long-range interactions becomes increasingly challenging. For the case $\alpha = 2$, these problems can be mitigated. Instead of a linear chain, we consider a triangular ladder such that each atom (away from the boundaries) has exactly 4 nearest neighbors with $d = 1$. This allows us to more efficiently implement the PPXPP model ($\alpha = 2$). We set $\Omega/2\pi = 2$ MHz and use $V_1/\Omega = 9$. We also use $\Delta/\Omega = 0.213$ instead of 0 to further suppress long-range interactions, see SM of Ref. [53]. The Hamiltonian in Eq. (A1) was used to produce the data in Fig. 4 using sparse Krylov methods.

Algebraic structure—For even values of K and for any α, we define the FSA raising operator J^+ as

$$J^+ = \sum_{j=0}^{N/K-1}\left[\sum_{l=1}^{K/2}\tilde{\sigma}^+_{Kj+l} + \sum_{l=K/2+1}^{K}\tilde{\sigma}^-_{Kj+l}\right]. \tag{B1}$$

This operator takes $|0\rangle_{K/2}$ to $|W\rangle_{K/2}$ in the first half of the cell and does the opposite in the second half. The lowering operator is $J^- = (J^+)^\dagger$. We can use these two operators to define $J^x = (J^+ + J^-)/2 = H_\alpha/2$. We can also define J^y as in Eq. (3) of the main text. We compute the J^z operator as $[J^x, J^y]/i$. Due to the form of J^x and J^y, J^z will only have diagonal terms of the form $\tilde{\sigma}^z$ as well as off-diagonal terms $\tilde{\sigma}^+_l\tilde{\sigma}^-_m + \tilde{\sigma}^-_l\tilde{\sigma}^+_m$. In general, these terms go from range-1, $\tilde{\sigma}^+_l\tilde{\sigma}^-_{l+1} + \tilde{\sigma}^-_l\tilde{\sigma}^+_{l+1}$, to range-$\alpha$, $\tilde{\sigma}^+_l\tilde{\sigma}^-_{l+\alpha} + \tilde{\sigma}^-_l\tilde{\sigma}^+_{l+\alpha}$. However, there can be cancellations between them for specific values of K. Indeed, if $K = 2\alpha$ or $K = 2\alpha+2$, the two halves of the cells are essentially disconnected and J^z simplifies to

$$J^z = \frac{1}{2}\sum_{j=0}^{N/K-1}\left[\left[\sum_{l=1}^{K/2} - \sum_{l=k+1}^{K}\right]\tilde{\sigma}^z_{Kj+l} + \left[\sum_{\substack{l,m=1\\ l<m}}^{K/2} - \sum_{\substack{l,m=K/2+1\\ l<m}}^{K}\right](\tilde{\sigma}^+_{Kj+l}\tilde{\sigma}^-_{Kj+m} + \tilde{\sigma}^+_{Kj+m}\tilde{\sigma}^-_{Kj+l})\right]. \tag{B2}$$

The XY-type terms act between all possible pairs of sites in the first half of the cell (with a $+1$ prefactor) and between all possibles pairs of sites in the second half of the cell (with a -1 prefactor). In SM [44] we show details for a few values of α and K, including cases where K is not between 2α and $2\alpha+2$.

For K odd, the J^+ operator has a similar structure, with $\tilde{\sigma}^+$ in the first half of the cell [first $(K-1)/2$ spins] and $\tilde{\sigma}^-$ in the second half, but the middle site now has an $\tilde{\sigma}^x/2$ operator. This preserves the fact that J^- can be obtained by applying spatial inversion to J^+, and that J^+ and J^- still sum to H. This implies that the J^y operator is as in the even K case (with $\tilde{\sigma}^y$ in the first half of the cell and $-\tilde{\sigma}^y$ in the second half) but without any operators acting on the middle site of the cell.

In the special case where $K = 2\alpha+1$, the J^z operator has a similar structure as for $K = 2\alpha$ and $K = 2\alpha+2$.

The same XY terms act in the first half of each cell (sites 1 to α) as in the second half (sites $\alpha+2$ to $2\alpha+1$). In addition, there are also XY terms between both halves of the cell and the middle site $\alpha+1$. These additional terms in J^z are formally written as

$$\frac{1}{4}\left[\sum_{l=1}^{\alpha}-\sum_{l=\alpha+2}^{K}\right](\tilde{\sigma}^{+}_{Kj+l}\tilde{\sigma}^{-}_{Kj+\alpha+1}+\tilde{\sigma}^{+}_{Kj+\alpha+1}\tilde{\sigma}^{-}_{Kj+l}), \quad \text{(B3)}$$

where we omitted the sum over unit cells $j=0$ to $N/K-1$.

Periodic MPS trajectories—A low dimensional manifold which can capture the scarring from the $|\mathbf{Z}_2\rangle$ and $|\mathbf{Z}_3\rangle$ states has previously been proposed for the PXP model [19,20]. It is based on parameterizing the wavefunction using a bond dimension $\chi=2$ matrix-product state (MPS) ansatz

$$A_j=\begin{pmatrix}\cos(\theta_j)|\downarrow\rangle & e^{i\phi_j}\sin(\theta_j)|\uparrow\rangle\\ |\downarrow\rangle & 0\end{pmatrix}. \quad \text{(C1)}$$

This ansatz can be thought of as a product of single-spin states on the Bloch sphere $\cos(\theta)|\downarrow\rangle+e^{i\phi}\sin(\theta)|\uparrow\rangle$, which is then projected into the constrained PXP space that allows no $|\ldots\uparrow\uparrow\ldots\rangle$ configurations. We can extend this ansatz to larger blockade radii α, with the bond dimension scaling as $\alpha+1$. This extended ansatz reads

$$A_j^{\alpha=2}=\begin{pmatrix}\cos(\theta_j)|\downarrow\rangle & 0 & e^{i\phi_j}\sin(\theta_j)|\uparrow\rangle\\ |\downarrow\rangle & 0 & 0\\ 0 & |\downarrow\rangle & 0\end{pmatrix}, \quad \text{(C2)}$$

and analogously for longer-range blockades. For all α and K satisfying $2\alpha\le K\le 2\alpha+2$, we find states in the manifold that have an overlap of over 97.8% with $|\mathrm{GS}_y\rangle$ and over 94.2% with $|\mathrm{GS}_z\rangle$ [for the system sizes used in Fig. 3(b), see SM [44] for details]. This last number rises to over 98.3% if we exclude the case $K=2\alpha+1$, highlighting the fact that the J^z operator we constructed for odd K is less accurate (see SM [44] for more details).

Crucially, we can always *exactly* represent the $|K\rangle$ states for $2\alpha\le K\le 2\alpha+2$ from Eqs. (2) and (4) as MPS states using the above ansatz for A_j^{α} with K different tensors A_j^{α} forming the unit cell. These tensors are completely specified by the values of the two angles (θ_j,ϕ_j). For $K=2\alpha$ or $K=2\alpha+2$, the θ angles read,

$$\theta_j=\begin{cases}0 & \text{if } j\le K/2,\\ a_{K+1-j} & \text{if } j>K/2,\end{cases} \quad \text{with} \quad \begin{array}{c}a_1=\pi/2,\\ a_k=\arctan(\sin(a_{k-1})).\end{array}$$

Meanwhile, all ϕ_j can be set to 0 as there is no phase difference depending on where the $|\uparrow\rangle$ are placed. The state $|K=2\alpha+1\rangle=\otimes_{j=1}^{M}[|0\rangle_\alpha\otimes|\tilde{W}_\beta\rangle_{\alpha+1}]$ is also contained in the MPS manifold. The first α angles and the last α angles have the same value as for the case $K=2\alpha$. For the middle site of the unit cell, the angle $\theta_{\alpha+1}$ is set to $\arctan(\beta\sin(\theta_{\alpha+2}))$, with the corresponding $\phi_{\alpha+1}$ angle being set to zero as well (assuming β is positive). We note however that the $|K\rangle$ state can also be compressed to bond dimension $\chi=2$ for $K\ge 2$ and $\chi=1$ for $K=2$.

The projection of the unitary dynamics generated by H_α onto the MPS variational manifold yields first order differential equations. Following the scheme in Ref. [20], equations of motion (EOMs) for the θ angles can be obtained from $\sum_j 2\,\mathrm{Im}\langle\partial_{\theta_j}\psi|\partial_{\phi_k}\psi\rangle\dot{\theta}_j=\partial_{\phi_k}\langle\psi|H_\alpha|\psi\rangle$ for all $k\in[1,K]$, where $|\psi\rangle$ is the MPS state with a unit cell of size K, depending on K variational θ and ϕ angles. The values of the ϕ angles are set to $\phi_j=\pi/2$ after differentiation is performed, since the plane with $\phi_j=\pi/2$ forms a flow-invariant subspace where $\dot{\phi}_j=0\ \forall\ j$.

Such EOMs were previously obtained in the PXP model for $K=2$ [19] and $K=3$ [20] unit cells, and we obtain them for $K=4$ (see SM [44]). We focus on the $|K\rangle$ state from Eq. (2) with $\alpha=1$, $K=4$ parameterized by angles $\theta_j=(0,0,\pi/4,\pi/2)$ and its trajectory in the classical phase space. We find that this point is located exactly on a periodic trajectory, as shown by the solid red line in Fig. 5(a). In addition, when perturbing the initial angles slightly, the resulting trajectory stays close to the periodic one at all times, indicating regular dynamics. A stability analysis of the periodic orbit confirms that it is stable with Lyapunov exponents being strictly zero up to numerical precision. Finally, the classical dynamics also allows us to

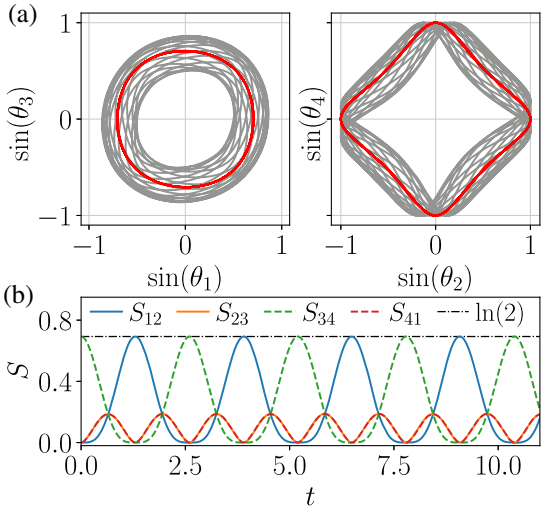

FIG. 5. (a) Dynamics in the space of the four angles parametrizing the MPS state after a quench from the K state shows a closed periodic trajectory (red). Dynamics initialized from a perturbed initial point near the periodic trajectory stays close to the original trajectory, suggesting its stability (gray). (b) The dynamics of entanglement entropy across different cuts on the periodic trajectory shows clear oscillations.

compute various properties of the physical system, such as entanglement entropy, which is shown in Fig. 5(b) for all nonequivalent bipartite cuts. The maximum entanglement entropy is ln(2), which occurs when the cut goes through the W part of a $|K\rangle$ state. This is in contrast with the PXP $\mathbf{Z}_2$ case, where the entanglement maximum occurs at the $|\mathrm{GS}_y\rangle$ state.

Beyond the PXP model, we also find EOMs for the $\alpha = 2$ and $K = 4$ case (see SM [44]), which also feature a periodic trajectory passing through the same initial point, $\theta_j = (0, 0, \pi/4, \pi/2)$. Figure 6(a) shows the entanglement dynamics on this trajectory. The exact entanglement dynamics in a long chain obtained with the time-evolving block decimation (TEBD) method shown in Fig. 6(b) show oscillations with the same period but with an added slow linear growth. This highlights that the projection onto the variational manifold is not exact, as it only captures the periodic behavior but not its gradual decay. After subtracting the linear growth, the entanglement oscillations in Fig. 6(c) agree well with entanglement on the variational trajectory, Fig. 6(a). As for the PXP $K = 4$ case, the maximum entanglement also occurs when a $|K\rangle$ state is cut in its W part. We expect this behavior to be identical for all α as long as $K > 2$.

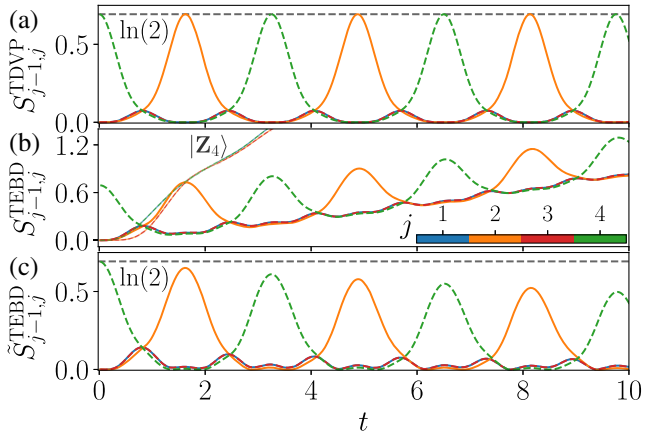

FIG. 6. Entanglement dynamics after a quench from $|K\rangle$ with $\alpha = 2$ and $K = 4$. (a) The periodic trajectory in the projected dynamics predicts infinite oscillations of the entanglement entropy. (b) Exact dynamics obtained using TEBD [59,60] for $N = 120$ sites, showing a linear ramp with oscillations on top. The growth of entanglement entropy is highly suppressed compared to the $|\mathbf{Z}_4\rangle$ case. (c) The entanglement entropy oscillations in the exact dynamics after subtracting the linear ramp show good agreement with the results in (a).